

# Neutron imaging detector based on the $\mu$ PIC micro-pixel chamber

J.D. Parker<sup>a,\*</sup>, K. Hattori<sup>a</sup>, H. Fujioka<sup>a</sup>, M. Harada<sup>b</sup>, S. Iwaki<sup>a</sup>, S. Kabuki<sup>a</sup>, Y. Kishimoto<sup>a</sup>, H. Kubo<sup>a</sup>, S. Kurosawa<sup>a</sup>, K. Miuchi<sup>a</sup>, T. Nagae<sup>a</sup>, H. Nishimura<sup>a</sup>, T. Oku<sup>b</sup>, T. Sawano<sup>a</sup>, T. Shinohara<sup>b</sup>, J. Suzuki<sup>b</sup>, A. Takada<sup>a</sup>, T. Tanimori<sup>a</sup>, K. Ueno<sup>a</sup>

<sup>a</sup>Department of Physics, Graduate School of Science, Kyoto University, Kitashirakawa-oiwakecho, Sakyo-ku, Kyoto 606-8502, Japan

<sup>b</sup>Materials and Life Science Facility Division, Japan Atomic Energy Agency (JAEA), Tokai, Ibaraki 319-1195, Japan

## Abstract

We have developed a prototype time-resolved neutron imaging detector employing the micro-pixel chamber ( $\mu$ PIC), a micro-pattern gaseous detector, coupled with a field programmable gate array-based data acquisition system for applications in neutron radiography at high-intensity neutron sources. The prototype system, with an active area of  $10 \times 10 \text{ cm}^2$  and operated at a gas pressure of 2 atm, measures both the energy deposition (via time-over-threshold) and 3-dimensional track of each neutron-induced event, allowing the reconstruction of the neutron interaction point with improved accuracy. Using a simple position reconstruction algorithm, a spatial resolution of  $349 \pm 36 \mu\text{m}$  was achieved, with further improvement expected. The detailed tracking allows strong rejection of background gamma-rays, resulting in an effective gamma sensitivity of  $10^{-12}$  or less, coupled with stable, robust neutron identification. The detector also features a time resolution of  $0.6 \mu\text{s}$ .

**Keywords:** neutron imaging, gaseous detector, micro-pattern detector

## 1. Introduction

The micro-pixel chamber ( $\mu$ PIC) [1], a type of micro-pattern gaseous detector [2], has been developed in our group at Kyoto University. The  $\mu$ PIC features a  $400\text{-}\mu\text{m}$  pitch with 2-dimensional strip readout coupled with a fast, compact FPGA (Field Programmable Gate Array)-based data acquisition system. The 2-dimensional measurement of the  $\mu$ PIC can be extended to three dimensions using an arrangement known generally as a time projection chamber (TPC). Detectors incorporating the  $\mu$ PIC have already been successfully developed for applications ranging from MeV gamma-ray astronomy [3] to medical imaging [4] to small-angle X-ray scattering [5]. By adding  $^3\text{He}$  to the gas mixture, such a system becomes an effective thermal neutron area-detector, well suited to neutron radiography at high-intensity neutron sources.

State of the art neutron radiography measurements require detectors capable of high spatial resolutions from several hundreds to tens of micrometers and a wide dynamic range for good image contrast. Commonly used neutron imaging detectors satisfying these requirements include imaging plates [6] and CCD (charge-coupled device)-based systems [7]. Imaging plates (IP) are capable of spatial resolutions down to  $25 \mu\text{m}$ , while CCD systems generally achieve resolutions around  $100 \mu\text{m}$ . Each of these detector types also features a wide dynamic range (on the order of  $10^5$ ) and good linearity in response to intensity. On the other hand, read-out times can be long, particularly in the case of IPs, which must be removed from the beam and scanned after each measurement. Another drawback of these integrating-type

detectors is a background proportional to measurement time, with no means of separating the neutron- and gamma-induced events.

To take full advantage of the new generation of high-intensity, pulsed spallation neutron sources and time-resolved radiographic techniques such as Bragg-edge transmission and resonance imaging, a detector which also possesses good time resolution and good discrimination against gammas is essential. At pulsed sources, the energy of an incident neutron is determined by measuring the time between the initiation of the pulse and the neutron's arrival at the detector (referred to as the time-of-flight, or TOF). This requires a time resolution generally on the order of microseconds. IPs are not suitable for measuring neutron TOF since typical exposure times are on the order of seconds or greater. In the case of CCDs, it is possible to achieve frame rates on the order of kHz (down to  $\sim 0.1 \text{ ms}$  per frame) [8], but the ability to measure neutron TOF remains limited. The gamma sensitivity of the IPs and CCDs is also an issue, since gammas are produced in copious amounts at spallation sources.

Our  $\mu$ PIC-based detector was able to overcome the limitations of IP and CCD systems, while maintaining many of their good characteristics. This stems from the fact that the  $\mu$ PIC is a counting-type detector (i.e., each neutron interaction is measured individually, or counted). Our prototype detector was able to assign a time for each event with a resolution down to  $0.6 \mu\text{s}$ , which is adequate for separating neutrons by TOF at pulsed sources. Also, examination of the properties of each event (track length, energy deposition, etc.) provided a powerful means for rejecting background on an event-by-event basis, resulting in an effective gamma sensitivity of  $\lesssim 10^{-12}$  while maintaining robust, stable neutron identification under varying

\*Corresponding author

Email address: jparkercr@scphys.kyoto-u.ac.jp (J.D. Parker)

detector conditions. The detailed event-by-event tracking also allowed our prototype neutron detector to achieve a spatial resolution of  $349 \pm 36 \mu\text{m}$ . The detector has a neutron detection efficiency of up to 35% for thermal neutrons with a peak efficiency of 75% for cold neutrons (from simulation).

For a similar  $\mu\text{PIC}$ -based X-ray imaging detector, a dynamic range comparable to IPs and CCD systems of  $10^5$  was observed [5], and with our prototype detector, good linearity versus incident intensity was confirmed for data rates up to 9 MHz (corresponding to  $\sim 1.5 \times 10^5$  neutrons/s) [9]. [The data rate in Ref. [9] (4.5 MHz) is quoted *per memory port* and should be multiplied by two for the total data rate.] The maximum data rate was limited by the data acquisition hardware and can be increased by as much as a factor of 10 or more (as described in Sec. 2.3). Furthermore, the  $\mu\text{PIC}$ , manufactured via inexpensive printed-circuit board technology, allows freedom to tailor the size and shape for a particular application, up to a maximum size of  $30 \times 30 \text{ cm}^2$ . Larger areas can be accommodated by tiling detectors, with dead space between the individual  $\mu\text{PIC}$ s as small as a few millimeters and, since the underlying anode structure remains unchanged, suffering no degradation in the operating characteristics with increasing area. Thus, our  $\mu\text{PIC}$ -based detector can combine a moderate spatial resolution, good time resolution, low gamma sensitivity, and large detection area with a wide dynamic range and high rate capability.

In the present paper, we describe the prototype detector and FPGA-based data acquisition system, as well as the analysis method for the resulting data. This is followed by a discussion of the gamma rejection capability, spatial resolution, and long-term operation of the detector.

## 2. Neutron imaging detector based on the $\mu\text{PIC}$

### 2.1. Detection method

Neutron detection was achieved via the absorption reaction,  ${}^3\text{He}(n, p){}^3\text{H}$ , which has a large cross-section for thermal neutrons (5,330 barns at  $E_n \approx 25.3 \text{ meV}$ ) and a Q-value of 764 keV. Owing to this large energy deposition and overall track lengths around 1 cm in the gas of the detector, the resulting proton-triton pairs were easily detected by the  $\mu\text{PIC}$  with gas gains as low as a few hundred. (For comparison, note that the  $\mu\text{PIC}$  has achieved stable operation for gas gains up to 6000 [10].) As typical neutron energies used in radiography measurements are negligible compared to the energy released in the detection reaction, the neutron interactions result in events with similar track lengths and energy deposition, allowing for easy separation from most backgrounds.

The negligible energy of the incident neutron also means the proton and triton emerge effectively back-to-back, but as the range of the proton is  $\sim 3$  times greater than that of the heavier triton (from simple kinematics), separation of the two particles is essential for an accurate determination of the neutron interaction point. By measuring the energy deposition *along* the track, the proton and triton can often be cleanly separated, facilitating a substantial improvement in spatial resolution. The feasibility of detecting neutrons with the  $\mu\text{PIC}$  and distinguishing protons and tritons via energy deposition was demonstrated

in a previous experiment [11]. In the prototype system, the energy deposit at each hit point was estimated using the time-over-threshold method, which measures the width (in time) of an analog pulse at a given threshold voltage [12]. Measuring the energy deposition in this way also gave another handle for rejecting background events.

### 2.2. Design of the prototype detector

For the current study, we constructed a dedicated neutron imaging detector prototype (shown in Fig. 1) based on a  $\mu\text{PIC}$  with an active area of  $10 \times 10 \text{ cm}^2$ . The  $\mu\text{PIC}$ , manufactured by Dai Nippon Printing Co., Ltd., Japan, consists of a  $100\text{-}\mu\text{m}$  thick polyimide substrate with copper cathode strips and anode pixels at a pitch of  $400 \mu\text{m}$ . The layout of the anodes and cathodes are shown in Fig. 2. Strips connecting the anodes on the underside of the substrate combine with the orthogonal cathode strips to produce a two-dimensional strip read-out. (See Ref. [1] for a detailed description of the  $\mu\text{PIC}$ .)

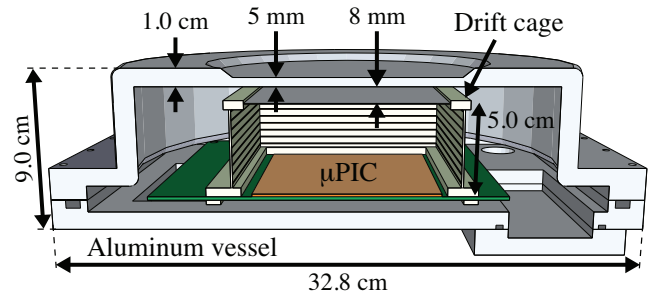


Figure 1: Diagram showing a cut-away of the neutron imaging detector prototype with a 5-cm tall drift cage.

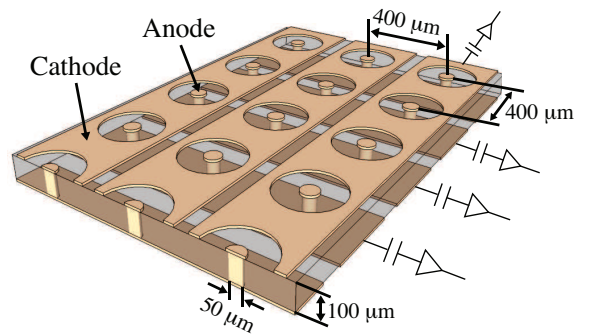


Figure 2: Schematic diagram of the  $\mu\text{PIC}$ . Anode pixels are connected on the backside by copper strips and, combined with the orthogonal cathode strips on the top-side, produce a 2-dimensional readout.

The active volume of the detector was created using a rectangular drift cage affixed above the  $\mu\text{PIC}$ , with sides constructed from G10 glass-reinforced epoxy laminate and topped with a drift plane consisting of  $0.3\text{-mm}$  thick aluminum sheet. The sides of the drift cage were etched with  $0.5\text{-mm}$  copper lines at a  $5\text{-mm}$  pitch, and the drift plane and each successive copper line were connected via a chain of  $50 \text{ M}\Omega$  resistors. Electric field strengths ranged from  $250 \sim 800 \text{ V/cm}$ , the optimum value depending on the particular gas mixture and pressure.

The  $\mu$ PIC and drift cage were contained within a sealed aluminum vessel with a 5-mm thick entrance window, outer dimensions of 32.8 cm  $\times$  32.8 cm  $\times$  9.0 cm, and a total gas volume of 2.5 L. The vessel could accommodate drift-cage heights up to 5 cm and was capable of withstanding gas pressures of over 2 atm. A 5-cm drift cage was used in the measurement of the spatial resolution described in Sec. 4.2, while the remaining data presented in this paper was taken with a 2.5-cm drift cage. The motivation for reducing the height of the drift cage will be elucidated in Sec. 4.2.

The filling gas consisted of Ar-C<sub>2</sub>H<sub>6</sub>-<sup>3</sup>He (63:7:30) at 2 atm. Our experience with  $\mu$ PIC-based detectors has shown that the above stopping gas and quencher (Ar-C<sub>2</sub>H<sub>6</sub> at 9:1) provide good gain and stability characteristics. For our initial detector study, we simply added <sup>3</sup>He to this standard mixture in a ratio providing adequate neutron detection efficiency. The pressure of 2 atm was chosen for increased efficiency and stopping power, while allowing the vessel and entrance window to remain relatively thin. The required drift field, 800 V/cm, was determined using the MAGBOLTZ program [13]. Optimization of the gas mixture for detection efficiency, spatial resolution, etc., will be the subject of a future study.

To estimate the neutron detection efficiency, and aide in our study of other detector properties, a simulation of the prototype detector was created using the GEANT4 software toolkit [14], and included the relevant physical processes (scattering, absorption, multiple scattering, electron diffusion, etc.). The simulation also emulated the response of the  $\mu$ PIC and data acquisition hardware to produce data identical in structure to the real system, which was then analyzed with the same software as the real data (described in Sec. 3). The GEANT4 simulation included the detector structures shown in Fig. 1 with the gas mixture and drift field described above.

Fig. 3 shows the calculated detection efficiencies as a function of neutron energy for the 5-cm (solid line) and 2.5-cm (dashed line) drift cages. The 5-cm drift cage gives a value of 35% for thermal neutrons ( $E_n \approx 25.3$  meV) and a peak efficiency of 75% at 0.7 meV. A drift height of 2.5 cm effectively halves the efficiency, resulting in a value of 18% for thermal neutrons. The large drop in efficiency below a neutron energy of about 1 meV in the 2.5-cm case is a result of absorption in the space between the entrance window and drift plane, resulting in an attenuation of the incident beam that increases with decreasing neutron energy. For comparison, the attenuation for the 5-cm drift cage with an 8-mm window-to-drift-plane gap is 13% at 0.7 meV, while that of the 2.5-cm cage (3.3-cm gap) is 74% at the same neutron energy. Reducing the height of the vessel to achieve the same window-to-drift-plane spacing as the 5-cm case would result in a peak efficiency of 65% at 0.35 meV (dotted line in Fig. 3).

### 2.3. Data acquisition system

In the data acquisition system (DAQ), the charge deposited on each anode and cathode strip, after being amplified by the  $\mu$ PIC, was read out through ASICs (Application-Specific Integrated Circuits) containing Amplifier-Shaper-Discriminators

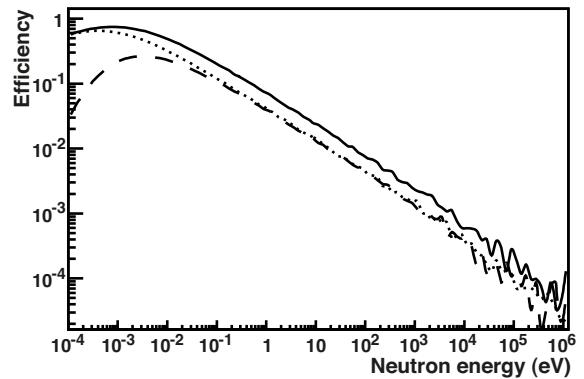


Figure 3: Expected neutron detection efficiency. Detection efficiency versus neutron energy as determined by a GEANT4 simulation is shown for the prototype detector with a 5-cm (solid line) and 2.5-cm (dashed line) drift height. The dotted line shows the efficiency for the 2.5-cm drift height when the window-to-drift-plane distance is equal to the 5-cm case.

(ASDs) [15]. The ASDs produce an LVDS (Low Voltage Differential Signaling) digital level whenever the analog signal from a strip crosses a common threshold voltage. These digitized signals were then sent to an FPGA encoder module to be synchronized with a 100-MHz internal clock and the position and time encoded into a 32-bit data word [16]. The encoded data was then sent over two 50-MHz parallel transfer lines to a VME memory module with a total capacity of 64 MB (16.8 Mwords), where they were read out to a PC and saved for further analysis.

This system was originally developed for use with low-rate  $\mu$ PIC-based gamma imaging detectors. In high-rate environments, the encoder-to-VME-memory transfer creates a bottleneck, limiting the maximum data rate to  $\sim 10$  MHz (1 Hz = 1 word/s). This maximum data rate could be increased an order of magnitude by employing multiple encoder modules transferring data directly to PC over Gigabit Ethernet. For example, using four such encoder modules (each handling 128 strips) would give an effective transfer rate of 4 Gb/s. This is equivalent to a data rate of 125 MHz, or a 12.5-fold increase.

The logic of the FPGA encoder was a key to the successful operation of our prototype detector. The version of the encoder logic used here, which simply encoded and streamed all incoming data, was designed for use at high-intensity X-ray or neutron sources where an event-by-event trigger is not practical. Additionally, each pulse from the  $\mu$ PIC produced not one, but two data words, one at the leading edge of the LVDS signal and a second at the trailing edge, marking each time the analog signal crossed the ASD threshold (as illustrated in Fig. 4). The resulting data words contained the strip number, the time relative to the internal clock of the encoder, and an *edge* bit used to indicate a leading or trailing edge. The time between these hit pairs, commonly referred to as *time-over-threshold* and referred to as *pulse width* herein, was determined in the offline analysis and, being a function of the pulse height, provided an estimate of the charge deposited on each strip [12]. Measuring the pulse widths in this way allowed for a more compact system and higher data rates than would be possible using conventional

ADCs for energy measurement. However, individual events had to be isolated from the data stream in the offline analysis.

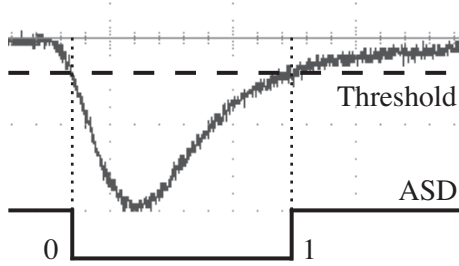


Figure 4: Illustration of FPGA encoder logic. An analog signal from the  $\mu$ PIC (oscilloscope trace) is superimposed with a representation of the ASD threshold level (dashed line) and ASD output signal (solid black line). The start (0) and end (1) times of the ASD signal are encoded in separate data words.

Fig. 5 shows a neutron interaction event measured using our prototype system. The position of the track, given by the relative time and strip number of each hit, is shown in Fig. 5(a), with the associated pulse widths shown in Fig. 5(b). The observed pulse-width distribution clearly displays the Bragg peaks of the stopping proton and triton and shows good agreement with the expected distribution, determined using our GEANT4 simulation and plotted in Fig. 6 (dashed histogram). While tracking alone gives no indication of the neutron interaction point, the proton and triton can be distinguished from the shape of the pulse-width distribution.

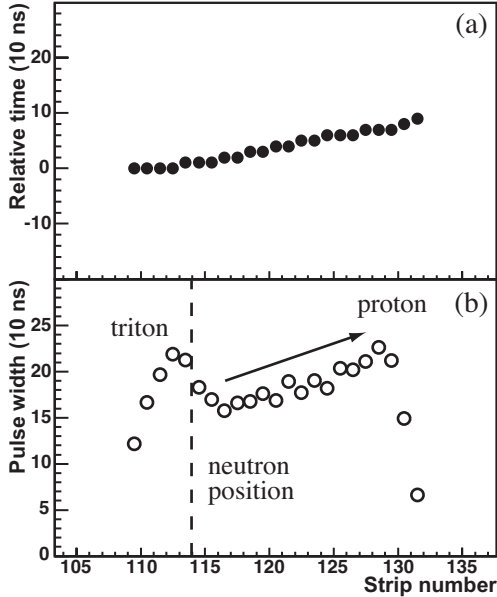


Figure 5: Proton-triton track measured with the prototype neutron detector. (a) Position (strip number) versus time and (b) pulse width for each hit strip are shown. The neutron interaction position (dashed line) and the slow rise of the proton Bragg peak (arrow) are indicated in (b).

### 3. Event reconstruction

The first task of the offline analysis was to cluster the raw hits from the data stream produced by the FPGA encoder into

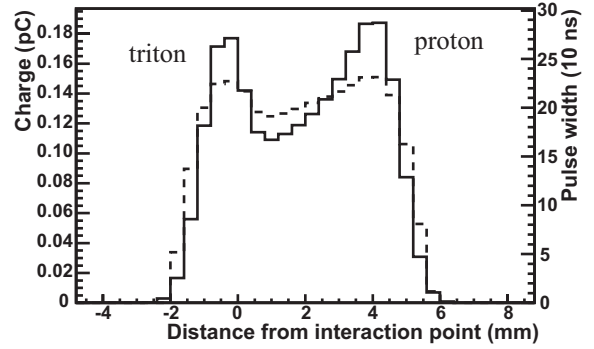


Figure 6: Simulation of pulse-width distributions. The charge deposition (solid line) and pulse-width distribution (dashed line) are shown for a proton-triton track as determined by our GEANT4 simulation.

individual events. This was accomplished in three steps: 1) match leading- and trailing-edge hit pairs and calculate pulse widths, 2) combine hits into anode and cathode clusters based on proximity in time and space, and 3) pair anode and cathode clusters based on proximity in time to make individual *events*. Once the events were reconstructed, interesting quantities such as the track length and pulse-width sum (for neutron identification) and the shape of the pulse-width distribution (for proton-triton separation) were evaluated as described below. The offline data analysis was carried out using software based on the ROOT object-oriented framework [17].

#### 3.1. Track-length determination

The 3-dimensional track length,  $l$ , was determined by combining the 2-dimensional hit positions measured by the  $\mu$ PIC with the hit-time information as:

$$l = \sqrt{(\Delta x - x_0)^2 + (\Delta y - y_0)^2 + v_d^2(\Delta t - t_0)^2}, \quad (1)$$

where  $\Delta x$  and  $\Delta y$  are the difference between the highest and lowest hit-strips for the anodes and cathodes, respectively, and  $\Delta t$  is the difference in the time of the earliest and latest hits which, when multiplied by the electron drift velocity,  $v_d$ , gives the component of the track length perpendicular to the  $\mu$ PIC. (The quantity  $\Delta t$  was determined separately for anodes and cathodes and then averaged.) The drift velocity was estimated using the MAGBOLTZ program [13] and had a value of  $v_d \approx 23 \mu\text{m/ns}$  for the 2-atm Ar-C<sub>2</sub>H<sub>6</sub>-<sup>3</sup>He (63:7:30) gas mixture and 800-V/cm drift field used here. The offsets  $x_0$ ,  $y_0$ , and  $t_0$  account for effects such as electron diffusion and decay time of the analog signals and were taken from the minimum measured values of  $\Delta x$ ,  $\Delta y$ , and  $\Delta t$ , respectively.

Fig. 7 shows the resulting track-length distribution for neutrons from a <sup>252</sup>Cf source moderated through loose-packed polyethylene pellets with an overall thickness of  $\sim 10$  cm. The expected distribution for thermal neutrons determined from our GEANT4 simulation is overlaid as the dashed histogram. The observed spread in the track-lengths of the proton-triton events is the result of multiple scattering and electron diffusion in the gas of the detector coupled with the finite strip pitch and non-zero ASD thresholds. The long tail extending to smaller track



lengths is mainly due to neutron events that were not fully contained within the active volume of the detector. The slight difference between the data and simulation is a result of uncertainties in the gains of the  $\mu$ PIC and ASD amplifiers, as well as the simplified model used to emulate the response of the ASDs in our simulation.

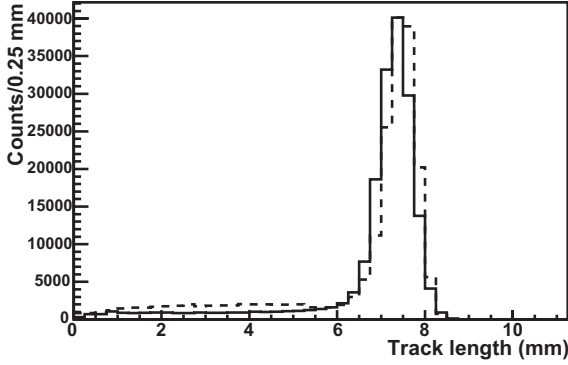


Figure 7: Distribution of track lengths. Track lengths for data taken with a moderated  $^{252}\text{Cf}$  source (solid) are shown with the expected distribution for thermal neutrons given by GEANT4 (dashed). The long tail is due to neutron events that were not fully contained in the detector.

A side effect of the streamed nature of the encoder data was that, while the relative distance between hits within a track could be calculated as described above, the absolute position of the track above the surface of the  $\mu$ PIC could not be determined. This was a direct result of the lack of a trigger reference time and lead to some uncertainty in the time for each event. The minimum uncertainty was determined from the time required for an electron cloud to drift across the entire drift height and has a value of about  $\pm 0.6 \mu\text{s}$  for the 2.5-cm drift cage and gas filling described in Sec. 2.2. The event-time uncertainty then increases as the velocity of the incident neutron decreases (to about  $3 \mu\text{s}$  for thermal neutrons at 2200 m/s and up to  $18 \mu\text{s}$  for 1-meV neutrons at 440 m/s, as determined by simulation). This effect dominates the timing resolution of our detector.

### 3.2. Pulse-width sum

The sum of pulse widths (or *total time-over-threshold*) was used as a rough estimate of total energy deposition. This was possible since the pulse widths are a function of the charge (and thus energy) deposited on each strip, as shown in Ref. [12]. For the purposes of the present analysis, it was not necessary to convert the widths to absolute charge or energy (i.e., that the relationship exists was sufficient, so that the pulse widths could take the place of energy deposition). This pulse-width sum, along with the track length described above, formed the basis for neutron identification.

The distribution of the pulse-width sum for the data taken with the moderated  $^{252}\text{Cf}$  source is shown in Fig. 8. The neutron events are clustered at higher values, producing the large peak seen in the plot. The small peak near the lower end is due to the gammas produced alongside the neutrons in the decay of  $^{252}\text{Cf}$ . The large width of the neutron peak arises from a dependence of the measured pulse widths on the angle of the

proton-triton track relative to the  $\mu$ PIC, and the long tail down to lower values is due to tracks that were not fully contained within the active volume of the detector. The data is in general agreement with the result of our GEANT4 simulation for thermal neutrons (overlaid on Fig. 8 as the dashed histogram), with slight differences due to the uncertainties in the gain and ASD response as mentioned in the previous section.

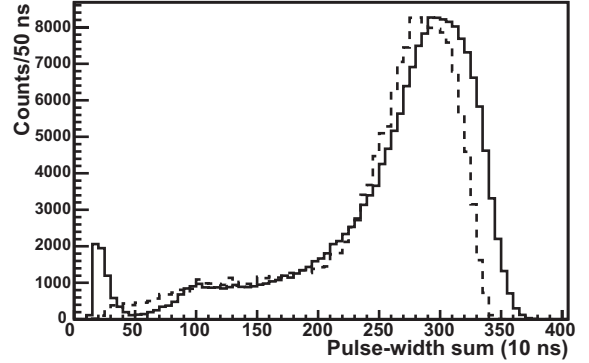


Figure 8: Pulse-width sum distribution. The pulse-width sum distribution for neutrons from a  $^{252}\text{Cf}$  source (solid) overlaid with the result of a GEANT4 simulation (dashed). The additional small peak seen in the data is due to the gammas produced along with the neutrons in  $^{252}\text{Cf}$  decay.

### 3.3. Proton-triton separation for position reconstruction

Proton-triton separation, essential for the accurate reconstruction of the neutron position, was carried out using the shape of the pulse-width distribution. As shown in Figs. 5(b) and 6, the triton deposits most of its energy in a relatively short distance, while the proton produces a gently sloping curve with the peak deposition near the stopping point (giving the familiar Bragg curve). The proton direction was then determined for the tracks which show this characteristic double-peaked shape in the pulse-width distribution by noting which end of the track displays the relatively slow rise of the Bragg curve of the proton, as indicated in Fig. 5(b).

Using our GEANT4 simulation, the efficiency of the proton-triton separation and determination of the proton direction, referred to as the PTS (proton-triton separation) efficiency, was estimated at  $\sim 95\%$  for tracks with angles  $\theta > 60^\circ$  and  $\phi_{a,c} > 30^\circ$  (for  $\theta$  and  $\phi_{a,c}$  as defined in Fig. 9). As the PTS procedure was performed for both the anode and cathode clusters, the PTS efficiency *per neutron event* becomes  $\sim 90\%$ . While the efficiency was roughly constant over the above range of angles, it dropped to zero for track angles  $\theta < 20^\circ$  or  $\phi_{a,c} < 10^\circ$ . This was due to the fact that, as one goes to smaller track angles, the electron cloud becomes concentrated over fewer and fewer strips, making it increasingly difficult to observe the double-peak structure. This was simply a limitation of the 2-dimensional strip readout and time-over-threshold methods used here.

After applying the PTS procedure, the corrected neutron interaction position,  $(X', Y')$ , was calculated as:

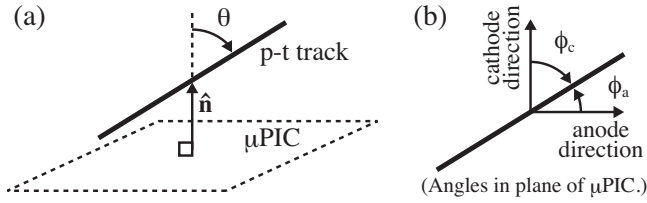


Figure 9: Definition of track orientation. The track orientation for an anode or cathode cluster is given by two angles: (a) the polar angle  $\theta$  defined relative to the normal to the plane of the  $\mu$ PIC, and (b) the azimuthal angle  $\phi_a$  ( $\phi_c$ ) defined relative to the anode (cathode) strip direction. All angles are restricted to the range 0 to 90 degrees.

$$\begin{aligned} X' &= X - \hat{x} \left( f_p - \frac{1}{2} \right) (\Delta x - x_0), \\ Y' &= Y - \hat{y} \left( f_p - \frac{1}{2} \right) (\Delta y - y_0), \end{aligned} \quad (2)$$

where  $X$  ( $Y$ ) is the mid-point of the proton-triton track for the anodes (cathodes) and  $\hat{x}$  and  $\hat{y}$  indicate the proton direction and take a value of +1 (−1) for a proton moving toward higher (lower) strip numbers or 0 if the proton and triton were not visible. The correction factor  $f_p = 0.785$  is the ratio of the proton track length to the total proton-triton track length and was determined using our GEANT4 simulation. The remaining terms give the  $x$  and  $y$  component of the total track length as described in Sec. 3.1. Neutron events for which the proton and triton could not be seen in either cluster (~15% of all events) should give the worst spatial resolution, while events in which they were visible in both clusters (~35%) should give the best. The improvement in the spatial resolution achieved by this method will be discussed in Sec. 4.2.

Another benefit of measuring the pulse-width distributions in this way relates to the background caused by fast neutrons (i.e., neutrons with energy on the order of MeV). These fast neutrons sometimes scatter with protons present in the materials of the detector, with a small fraction producing tracks with similar length and total energy deposit as the proton-triton tracks. The pulse-width distribution shown in Fig. 10 is one such scattered proton track, as measured with our prototype detector. Possessing no triton Bragg peak, the shape of the distribution is quite distinct from that of the proton-triton track of Fig. 5(b), providing the only means to reject such events.

## 4. Results and discussion

### 4.1. Neutron-gamma separation

Since the energy deposition for gamma events was near our detection threshold, the gamma detection efficiency, or the probability a gamma will interact in the detector and deposit enough energy in the active volume to produce data, was sensitive to the gain setting of the  $\mu$ PIC. This was in contrast to neutron events, which, being well above threshold, had a detection efficiency with virtually no gain dependence. To demonstrate this, the detector was irradiated simultaneously with a 1-MBq  $^{137}\text{Cs}$  gamma source placed in the center of the entrance window (giving an effective dose-rate of about 16  $\mu\text{Gy/h}$  over the

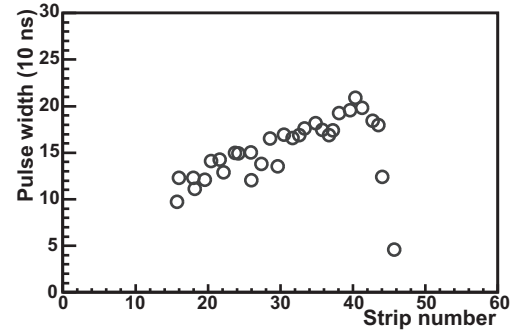


Figure 10: Scattered proton track measured with the prototype detector. Pulse width distribution for a proton scattered from the quencher gas by a fast neutron.

active volume) and a  $^{252}\text{Cf}$  source, emitting  $\sim 2 \times 10^4$  neutrons/s, located about 14 cm directly above the center of the entrance window, and moderated through  $\sim 10$  cm of polyethylene (consisting of pellets of size  $\sim 4$  mm). The detector was outfitted with a 2.5-cm drift cage and filled with  $\text{Ar-C}_2\text{H}_6\text{-}^3\text{He}$  (63:7:30) at 2 atm. The gas gain was controlled by altering the voltage applied to the anodes of the  $\mu$ PIC, and data was taken for 45 minutes at each gain setting. The results, normalized to counts per second, are shown in Fig. 11.

The upper plot of Fig. 11 shows the pulse-width sum distributions for several different gain settings, and the lower plot gives the corresponding neutron (squares) and gamma (open circles) rates. For the lower plot of Fig. 11, the neutrons and gammas were separated by an ‘energy’ cut in the pulse-width sum, with events above the cut considered neutrons and those below considered gammas. The total gamma rate decreased by nearly two orders of magnitude between the highest and lowest gain settings, while the total neutron rate remained virtually constant (total rates indicated by solid lines). Also shown are the effective neutron and gamma event rates after applying a track-length cut of  $-2\sigma$  to  $+3\sigma$  (dashed lines), where  $\sigma$  is the Gaussian width of the track-length distribution of Fig. 7, or after applying a PTS cut requiring the separation of the proton and triton in both the anode and cathode clusters of each event (dotted lines). These tracking cuts resulted in even larger reductions in the gamma event rate.

To further quantify the effectiveness of gamma rejection via track properties, more data was taken with the  $^{137}\text{Cs}$  source at a gain setting of  $\sim 600$ . (This gain setting provided a high enough count rate such that the measurement could be completed in a reasonable time and is similar to the gain setting used for the measurement of Sec. 4.2.) Using the same detector setup and gas filling as above, data was collected for 24 and 48 hours with and without the source, respectively. The resulting pulse-width sum distributions, normalized to counts per hour, are shown in Fig. 12(a) after the  $-2/+3\sigma$  track-length cut and Fig. 12(b) for both the track-length and PTS cuts. The distributions from  $^{137}\text{Cs}$  (open circles) are overlaid with the no-source distributions (closed circles). The large peak is due to thermal neutrons produced by cosmic rays, while the gammas from the  $^{137}\text{Cs}$  source are clearly visible as the smaller peak near the lower part of the distributions. The plots in Figs. 12(c) and (d) show the

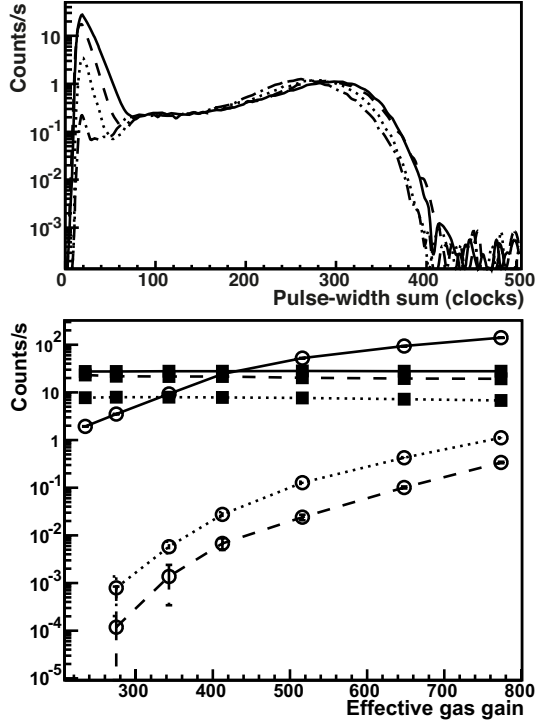


Figure 11: Neutron and gamma event rates as a function of gas gain. The upper plot shows the pulse-width sum at gain settings of 650 (solid line), 510 (dashed line), 345 (dotted line), and 230 (dash-dotted line). In the lower plot, the numbers of neutrons (squares) and gammas (open circles) detected per second are shown for: 1) no tracking cuts (solid lines), 2) with a track length cut (dashed lines), and 3) with the PTS cut (dotted lines) as described in the text.

results from our GEANT4 simulation for neutron, gamma, and cosmic-ray muon events for the same cuts as Figs. 12(a) and (b), respectively. The simulated data reproduces the features seen in the real data quite well.

The gamma contamination for a given set of tracking cuts was found by integrating the pulse-width sum distributions above the ‘energy’ cutoff indicated in Fig. 12 and subtracting the number of background counts observed for the same conditions. The resulting negative numbers, as shown in Table 1, are due to variations in the background cosmic-ray rate, limited statistics due to the overall low background rate, and slight variations in the  $\mu$ PIC gain over time. In light of this, the final results are given as upper limits determined in a way that accounts for the physical constraint that the rates cannot be less than zero [18]. After normalizing to the total number of gammas detected per hour, gamma contamination fractions of  $< 9.3 \times 10^{-6}$  and  $< 3.6 \times 10^{-6}$  (95% confidence level) were found for the data shown in Figs. 12(a) and 12(b), respectively. Taking into account the gamma detection efficiency at the above gain setting ( $\sim 6 \times 10^{-4}$ ), a gamma sensitivity on the order of  $10^{-9}$  or less was determined for our prototype detector when operated at a gain of  $\sim 600$ . Furthermore, from the results of Fig. 11 for the gamma rates after track length and PTS cuts, we estimated that a decrease in the gas gain to around 275 would reduce the gamma sensitivity by another three orders of magnitude, resulting in an effective gamma sensitivity on the order of  $10^{-12}$  or

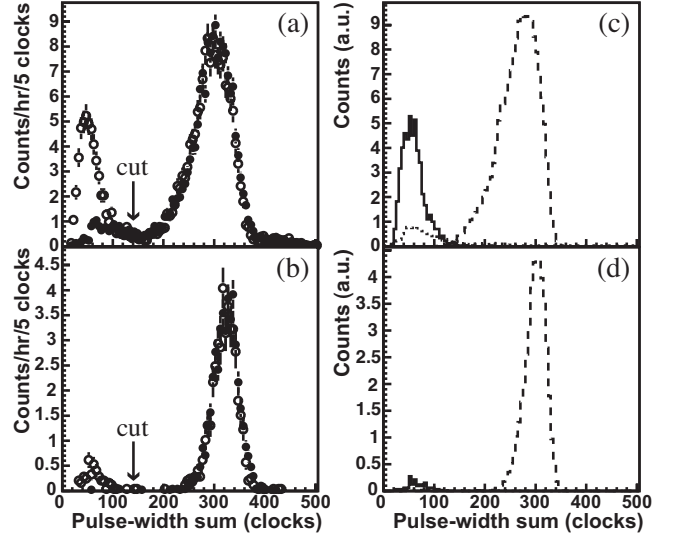


Figure 12: Neutron-gamma separation. Pulse-width sums for events from a  $^{137}\text{Cs}$  source (open circles) and with no source (closed circles) are shown for (a) track-length cut only and (b) track-length and PTS cuts. Plots (c) and (d) show simulated data, including 662-keV gammas (solid line), neutrons (dashed line), and cosmic-ray muons (dotted line), for the same cut conditions as (a) and (b), respectively. The ‘gamma cut’ at 140 clocks is also indicated.

less with no change in neutron efficiency.

For comparison, we consider  $^3\text{He}$  tubes, which, while not suitable for high-resolution imaging, provide the best neutron-gamma separation among commonly used detectors. Owing to the detailed tracking capabilities of our detector, the effective gamma sensitivity found above is on par or better than that of  $^3\text{He}$  tubes (see for instance, Ref. [19]), which separate neutrons and gammas via pulse-height only. (Due to differing experimental conditions and detector geometries, it is difficult to make a direct comparison.) Furthermore, the neutron identification efficiency for a  $^3\text{He}$  tube can have a strong dependence on the operating voltage, which must be optimized to obtain acceptable gamma rejection at a given background rate (see Ref. [20] for typical  $^3\text{He}$ -tube plateau curves). This is in contrast to the present results of Fig. 11 (lower plot), which show excellent stability for neutron identification versus gas gain.

#### 4.2. Spatial resolution

The spatial resolution of the prototype detector was studied using a cadmium test chart. The data were taken in November 2009 at the Japan Spallation Neutron Source (JSNS) located at the Japan Proton Accelerator Research Facility (J-PARC) in Tokai, Japan. The measurements were carried out at NOBORU (NeutrOn Beamline for Observation and Research Use) [21], with a beam power at the time of the experiment of  $\sim 100$  kW. The prototype detector was filled with the same gas mixture as in the previous section and operated at a gas gain around 600, and a 5-cm drift cage was installed above the  $\mu$ PIC. The detector was placed in the beam at a distance of 14.5 m from the moderator, and the cadmium test chart, of size  $50 \times 50$  mm<sup>2</sup>, was attached directly to the entrance window.

The resulting images, shown in Fig. 13, were taken with an exposure time of 9.2 minutes at a neutron rate of  $\sim 42$  kcps. The

Table 1: Gamma rejection with tracking cuts for irradiation with a 1-MBq  $^{137}\text{Cs}$  source. Data are given in counts/hour. The contamination fraction is the ratio of the contamination rate for a given set of cuts to the contamination rate with no cuts. Upper limits (given in parentheses) are at the 95% confidence level.

Cuts	$^{137}\text{Cs}$	No source	Contamination	Contamination fraction
None	$351360 \pm 120$	$3700.4 \pm 8.8$	$347660 \pm 120$	1
Track length	$185.0 \pm 2.7$	$161.1 \pm 1.8$	$23.9 \pm 3.3$	$6.87 \times 10^{-5}$
Energy	$284.2 \pm 3.4$	$290.1 \pm 2.5$	$-5.8 \pm 4.2 (< 3.65)$	$(< 1.0 \times 10^{-5})$
Track length $\wedge$ Energy	$145.6 \pm 2.4$	$148.7 \pm 1.8$	$-3.2 \pm 3.0 (< 3.22)$	$(< 9.3 \times 10^{-6})$
Track length $\wedge$ Energy $\wedge$ PTS	$43.4 \pm 1.3$	$46.1 \pm 1.0$	$-2.7 \pm 1.7 (< 1.24)$	$(< 3.6 \times 10^{-6})$

numbers of events remaining after each tracking cut are listed in Table 2. The TOF cut (equivalent to a neutron energy cut of  $E_n < 0.12$  eV) selected neutrons with energy well below the cadmium cut-off, and the looser energy and track length cuts, as compared to the previous section, were possible due to the minimal gamma contamination in the selected TOF region. The final images were normalized to the beam profile measured with no sample present (at similar statistics).

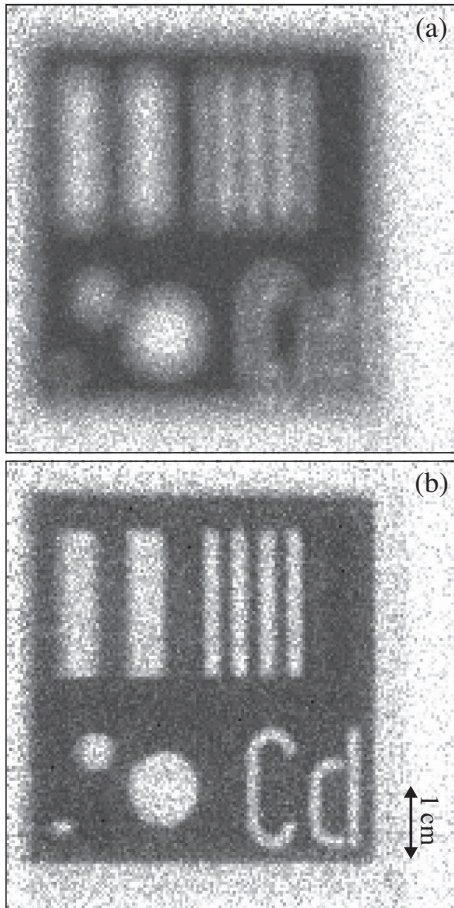


Figure 13: 2-dimensional images of a cadmium test chart. (a) Image with neutron positions determined as the mid-point of the proton-triton tracks. (b) Image with corrected neutron positions after proton-triton separation. Lighter areas indicate higher neutron transmission.

For the image in Fig. 13(a), the pulse-width information was disregarded, and the neutron position was taken as the mid-

Table 2: Data for image of Cd test chart. The number of beam pulses and total number of events included in the present analysis are given. Also shown are the numbers of events remaining after each subsequent tracking cut.

	Number	Fraction	Note
Beam pulses	13871	–	
Events	$2.35 \times 10^7$	–	
TOF > 3 ms	$3.38 \times 10^6$	1	
Energy > 50 clocks	$3.35 \times 10^6$	0.99	
Track length ( $\pm 3\sigma$ )	$2.85 \times 10^6$	0.84	Fig. 13(a)
PTS cut	$9.90 \times 10^5$	0.29	Fig. 13(b)

point of the proton-triton track ( $X, Y$  in Eq. 2). The resolution was estimated by fitting the projection of a straight edge (sometimes referred to as a *knife-edge target*) with the function:

$$N(x) = \frac{A}{2} \left[ 1 - \operatorname{erf} \left( \frac{x - \mu}{\sqrt{2}\sigma} \right) \right] + C, \quad (3)$$

derived assuming a Gaussian resolution, where  $A$  is a normalization factor,  $\operatorname{erf}()$  is the usual Gaussian error function,  $\mu$  is the mean position of the edge,  $\sigma$  is the corresponding Gaussian width, and  $C$  is a constant. Using the right-most vertical edge of the test chart, the resolution was found as  $\sigma = 990 \pm 180 \mu\text{m}$ . This is in good agreement with a previous test experiment carried out by our group in September 2008 at the NOP beamline of the JRR-3 reactor in Tokai, Japan, using a  $\mu\text{PIC}$ -based X-ray imaging detector modified to detect neutrons (by adding a small amount of  $^3\text{He}$  to the usual gas mixture) [22]. This previous experiment, which used an older version of the FPGA firmware without the time-over-threshold measurement capability, found a spatial resolution of about  $956 \mu\text{m}$ . (The  $\mu\text{PIC}$  and DAQ hardware were essentially identical to that used for the current prototype.)

Using the pulse-width information available in the current data, the image quality was greatly improved (Fig. 13(b)) by separating the proton and triton and calculating the neutron interaction points via Eq. 2. The spatial resolution was again determined via Eq. 3 and was found to be  $\sigma = 349 \pm 36 \mu\text{m}$ , representing an improvement by a factor of 2.8. To achieve this spatial resolution, the events were limited to those in which the proton and triton were visible in both the anode and cathode clusters (PTS cut). As discussed in Sec. 3.3 (and confirmed in Table 2), such events account for only about 35% of all neutron



events, resulting in a combined neutron efficiency for the image of  $\sim 10\%$  for thermal neutrons. When all events passing the energy and track-length cuts are included in the image, the spatial resolution becomes  $523 \pm 39 \mu\text{m}$ , which, although still an improvement over the case with no position correction, is about 50% worse than the best resolution. Thus, a trade-off must be made between resolution and efficiency.

The distortion apparent on the left side of Fig. 13(b) is a result of beam divergence, which produces a smearing of the image that increases with the distance from the beam center. As with the time resolution discussed in Sec. 3.1, this was a result of our inability to measure the absolute position of an event above the surface of the  $\mu\text{PIC}$ . While the effect is clearly visible on the left of the image, it was estimated via simulation to increase the observed spatial resolution by only about 1% at the edge used in the above determination (well within errors). This smearing can be reduced by optimizing the beam geometry to minimize divergence and by decreasing the drift height to reduce the uncertainty in the interaction position. The latter point led us to change from the 5-cm drift cage to the 2.5-cm cage used in previous sections.

Improvement of the spatial resolution can be attained with more sophisticated position reconstruction algorithms incorporating the shape of the pulse-width distribution (as in Ref. [12] for X-ray imaging with the  $\mu\text{PIC}$ ). Preliminary results for our neutron detector suggest nearly a factor of 3 improvement in the resolution is possible [23]. Further improvement is expected through optimization of the gas mixture and pressure, although, according to our GEANT4 simulation, the spatial resolution is ultimately limited to between 90 and 100  $\mu\text{m}$  by the underlying pixel-pitch. Our simulation showed that this maximal value is achieved for a gas mixture with a diffusion constant about half the current mixture or one with a track length around 5 mm. For the latter, shorter track lengths (down to a minimum of  $\sim 3$  mm for which the proton and triton can be effectively separated) would reduce the amount of data per event but would also yield a smaller range of usable track angles and a reduced reconstruction efficiency. A trade-off is thus affected between spatial resolution, efficiency, and maximum neutron rate. These ongoing studies will be explored in a subsequent paper.

#### 4.3. Long-term operability and $^3\text{He}$ usage

At a time when the demand for  $^3\text{He}$  is already outstripping the world's supply [24], it is important to consider the  $^3\text{He}$  usage of the detector. Over time, various processes, such as dissociation of the quencher gas and outgassing from the materials of the detector, lead to a buildup of impurities and a degradation in the properties of the gas. To maintain the desired gas properties, the detector must be periodically evacuated and refilled. To date, the prototype detector has been filled two times with the gas mixture described in this paper. The first filling was used for a period of 13 months, and the second has been used up to the present ( $\sim 14$  months). The gas gain slowly diminished over each fill period, decreasing by 68% during the first and by 30% during the second. Also, the initial value of the second filling was 56% that of the first, perhaps indicating some additional aging process of the  $\mu\text{PIC}$ . In each case, however, sufficient gain

for neutron detection could still be attained by increasing the anode voltage setting, with no significant change observed in detector performance over time.

A one-year fill cycle is already long when compared to other  $\mu\text{PIC}$  applications, which, due to the need to operate at much higher gains, must be refilled every few months. By treating the vessel and  $\mu\text{PIC}$  against outgassing through annealing (not done for our prototype) and employing a gas filtration system, such as one now under development in our group at Kyoto University [25], it should be possible to stabilize the gas gains over time and extend the operation of the detector significantly. If these improvements can be realized, the yearly costs for detector maintenance would be greatly reduced.

## 5. Conclusion

We have developed a time-resolved neutron imaging detector based on the  $\mu\text{PIC}$  micro-pixel chamber. By measuring the energy deposition (via time-over-threshold) and track positions, we were able to demonstrate a small effective gamma sensitivity of  $\lesssim 10^{-12}$  and neutron identification that was stable and robust. A spatial resolution of  $\sim 350 \mu\text{m}$  was achieved, with significant improvements expected through the use of more sophisticated reconstruction algorithms and optimization of the gas mixture. A time resolution as low as 0.6  $\mu\text{s}$  allows for clean separation of neutrons by time-of-flight at pulsed neutron sources. The detector, operated at a moderate pressure of a few atmospheres, was able to maintain its good operating characteristics for more than one year on a single gas filling. The compact FPGA-based data acquisition system is simple to setup and operate and, although limited to a maximum neutron rate of  $\sim 150$  kcps, could potentially support a rate 10 times that by upgrading the encoder-to-PC data transfer method. Furthermore, the printed-circuit board manufacturing process is inexpensive and allows some freedom to choose the size and shape of the  $\mu\text{PIC}$  to suit a particular experiment (up to a maximum size of  $30 \times 30 \text{ cm}^2$ ), and larger areas can be covered by tiling detectors with no degradation in the operating characteristics with increased area. These properties make the  $\mu\text{PIC}$  an attractive solution for neutron imaging applications requiring very low background, time-resolved measurements, and the ability to cover large areas at moderate resolution.

## Acknowledgements

This work was supported by the Quantum Beam Technology Program of the Japan Ministry of Education, Culture, Sports, Science and Technology (MEXT). The authors would like to thank the staff at J-PARC and the Materials and Life Science Facility for providing a stable neutron beam during our test experiment in November 2009.

## References

- [1] A. Ochi et al., Nucl. Instr. and Meth. A 471 (2001) 264.
- [2] A. Oed, Nucl. Instr. and Meth. A 263 (1988) 351.
- [3] A. Takada et al., Nucl. Instr. and Meth. A 546 (2005) 258.

- [4] S. Kabuki et al., Nucl. Instr. and Meth. A 580 (2007) 1031.
- [5] K. Hattori et al., J. Synchrotron Rad. 16 (2009) 231.
- [6] H. Kobayashi and M. Satoh, Nucl. Instr. and Meth. A 424 (1999) 1.
- [7] H. Pleinert et al., Nucl. Instr. and Meth. A 399 (1997) 382.
- [8] M. Matsubayashi et al., Nucl. Tech. 132 (2000) 309; P. Vontobel et al., Nucl. Instr. and Meth. A 542 (2005) 148.
- [9] J.D. Parker et al., 2010 IEEE Nuclear Science Symposium Conference Record (©2010 IEEE) 291.
- [10] M. Bouianov et al., Nucl. Instr. and Meth. A 540 (2005) 266.
- [11] T. Tanimori et al., Nucl. Instr. and Meth. A 529 (2004) 236.
- [12] K. Hattori et al., Nucl. Instr. and Meth. A 674 (2012) 1.
- [13] S.F. Biagi, Nucl. Instr. and Meth. A 421 (1999) 234.
- [14] S. Agostinelli et al., Nucl. Instr. and Meth. A 506 (2003) 250; J. Allison et al., IEEE Trans. Nucl. Sci. 53 (2006) 270.
- [15] R. Orito et al., IEEE Trans. Nucl. Sci. 51 (2004) 1337.
- [16] H. Kubo et al., 2005 IEEE Nuclear Science Symposium Conference Record (©2005 IEEE) 371.
- [17] R. Brun and F. Rademakers, Nucl. Instr. and Meth. A 389 (1997) 81. See also <http://root.cern.ch/>.
- [18] G.J. Feldman and R.D. Cousins, Phys. Rev. D 57 (1998) 3873.
- [19] R.T. Kouzes et al., Nucl. Instr. and Meth. A 654 (2011) 412.
- [20] D.H. Beddingfield, N.H. Johnson, and H.O. Menlove, Nucl. Instr. and Meth. A 455 (2000) 670.
- [21] F. Maekawa et al., Nucl. Instr. and Meth. A 600 (2009) 335.
- [22] K. Hattori, Doctoral thesis, Kyoto University (2009).
- [23] J.D. Parker et al., 2011 IEEE Nuclear Science Symposium Conference Record (©2011 IEEE) 393.
- [24] R.T. Kouzes, *The <sup>3</sup>He Supply Problem*, Technical Report PNNL-18388, Pacific Northwest National Laboratory, Richland, WA, 2009.
- [25] K. Nakamura et al., JINST 7 (2012) C02023.